Temporal Characterization of Femtosecond Laser-Plasma-Accelerated Electron Bunches Using Terahertz Radiation

J. van Tilborg,[1,*] C. B. Schroeder,[1] C. V. Filip,[2] Cs. Tóth,[1] C. G. R. Geddes,[1] G. Fubiani,[1,†] R. Huber,[1] R. A. Kaindl,[1] E. Esarey,[1,2] and W. P. Leemans[1,2]

[1]*Lawrence Berkeley National Laboratory, University of California, Berkeley, California 94720, USA*
[2]*University of Nevada, Reno, Nevada 89557, USA*

(Received 1 July 2005; published 4 January 2006)

The temporal profile of relativistic laser-plasma-accelerated electron bunches has been characterized. Coherent transition radiation at THz frequencies, emitted at the plasma-vacuum boundary, was measured through electro-optic sampling. Frequencies up to the crystal detection limit of 4 THz were observed. Comparison between data and theory indicates that THz radiation from bunches with structure shorter than $\simeq 50$ fs (root-mean-square) is emitted. The measurement demonstrates both shot-to-shot stability of the laser-plasma accelerator and femtosecond synchronization between bunch and probe beam.

DOI: 10.1103/PhysRevLett.96.014801 PACS numbers: 29.25.Bx, 41.60.−m, 52.38.Kd

Laser-driven plasma-based accelerators [1–9] are of great interest to the scientific community because of the ultrahigh accelerating gradients generated, and the high-brightness electron bunches that are produced. In such an accelerator, a focused intense ($>10^{19}$ W cm^{-2}) laser pulse drives a plasma density wave, oscillating at the plasma frequency. For a sufficiently large amplitude wave, plasma electrons can be trapped and accelerated to relativistic energies. Accelerating gradients on the order of 10–100 GV m^{-1} and generation of multi-nC electron bunches have been demonstrated [3–9]. Simulations and theory [10,11] indicate that the electron bunches are intrinsically short and dense since the transverse bunch size is on the order of the laser spot size (~ 10 μm), and the bunch length is on the order of the plasma wavelength (typically 5–20 μm, depending on the plasma density). The laser, the relativistic electrons, and secondary radiation such as γ rays [12], x rays [13,14], and THz waves [15–17] are intrinsically synchronized in time. The compact accelerator size, the ultrashort electron bunch generation, and the synchronized radiation emission open a broad perspective for future scientific experiments.

Temporal characterization of electron beams produced by conventional accelerators has been performed either by analyzing the direct Coulomb field of the bunch [18–22], or by characterizing coherent transition radiation (CTR) [23–25]. CTR is emitted by the electron bunch as it propagates from one medium to another [26], e.g., through a metallic foil. Note that CTR measurements at conventional accelerator facilities have generally focused on the angular and spectral intensity distribution rather than on the direct (electric field) CTR waveform. For the laser-plasma accelerator [also referred to as laser-wakefield accelerator (LWFA)], the plasma-vacuum interface acts as the CTR media transition and LWFA-produced CTR at THz frequencies has been measured [15–17,27]. Previous CTR experiments on LWFA-produced electron bunches have focused on measuring THz pulse energy and polarization [15], and two energy measurements in different spectral ranges of detector acceptance suggested the existence of sub-100 fs bunch structure [27]. However, to date, neither extensive spectral analysis, nor temporal characterization of the THz pulse and the LWFA electron bunch profile have been realized.

In this Letter we report on direct THz waveform measurements (amplitude and phase), obtained with an electro-optic (EO) sampling technique [18–22,28–30], performed to derive temporal properties of the LWFA electron beam. Through the EO effect, the THz waveform induces a change in birefringence of a crystal, proportional to the THz electric field strength and sign, which is then probed by a femtosecond laser beam (probe beam). By scanning the delay between the THz pulse and probe beam, a full THz waveform was recorded. This measurement also demonstrates LWFA stability and applicability in pump-probe type of experiments.

The experiments were performed with the high-power Ti:Al_2O_3 laser of the LOASIS facility at the Lawrence Berkeley National Laboratory [27]. A schematic of the experimental configuration is shown in Fig. 1. A Ti:Al_2O3 laser beam (wavelength of $\lambda_0 = 800$ nm) was focused [spot size $\simeq 3.6$ μm root-mean-square (rms)] by an off-axis parabola (OAP1) onto Helium gas emerging from a gas jet (diameter of 2 mm) with a backing pressure of 1000 psi. The peak electron density in the plasma was 3×10^{19} cm^{-3}, corresponding to a plasma wavelength of $\lambda_p = 6$ μm. The total charge of the electron bunch was $\simeq 2.4$ nC (measured 50 cm from the gas jet). The electron energy distribution $g(E)$, measured by a magnetic spectrometer and averaged over multiple shots, showed an exponential form of $g(E) \sim \exp(-E/E_t)$, with $E_t = 5$ MeV. Part of the THz radiation was collected and collimated by an $F/2$ 90°-off-axis parabola (OAP2, 15 cm focal length), positioned off center ($\theta = 19°$ with respect to the main propa-

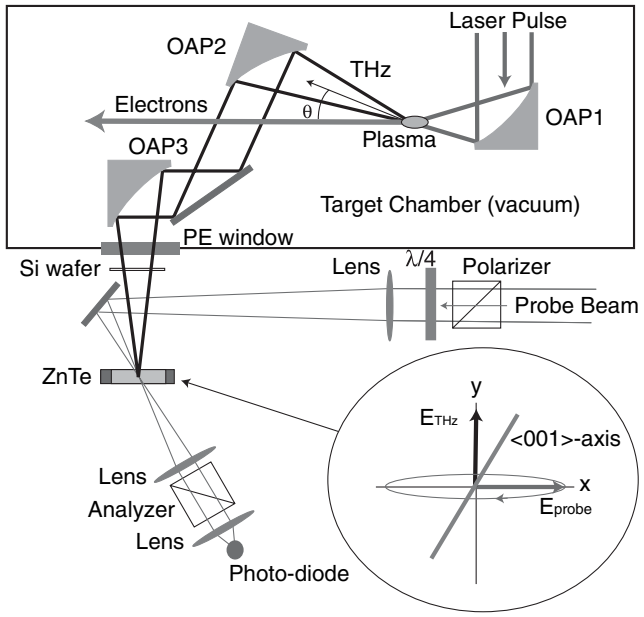

FIG. 1. Schematic representation of the LWFA, the THz (CTR) beam path, and the EO detection setup.

gation axis) to avoid damage from the electron or laser beams. The collimated THz radiation was then focused by an $F/2.4$ 90°-off-axis parabola (OAP3, 18 cm focal length) onto a 200 μm-thick ZnTe crystal, positioned outside the target chamber [a 3.2 mm-thick polyethylene (PE) disk served as window]. A high-resistivity Si wafer blocked remnant laser light from interfering with the EO detection. A 21 fs (rms) Ti:Al_2O_3 probe beam, split off from the main laser beam to provide synchronization, was focused (spot size <20 μm) to overlap with the THz beam in the ZnTe crystal. A polarizer ensured horizontal polarization of the probe beam, while the analyzer was rotated to transmit only the vertical component to a biased photo-diode. The ZnTe crystal was cut in the $\langle 110 \rangle$ plane, and the $\langle 001 \rangle$ axis was rotated to optimize the signal-to-noise ratio of the EO measurement. The electric field vectors of the probe beam and THz pulse are shown in the bottom right of Fig. 1. Although the emitted THz pulse is radially polarized [16], OAP2 selects a specific polarization component which corresponds to vertical polarization at the crystal surface.

With future single-shot EO experiments as a motivation, single-diode detection of the probe beam [31] was preferred over balanced-diode detection [28]. To resolve the sign of the THz pulse, a quarter-wave plate ($\lambda/4$ plate) was used to provide the necessary ellipticity to the probe beam polarization. It has been shown [31] that in this experimental configuration (sign-resolved single-diode EO sampling), the best signal-to-noise ratio is obtained with a small rotation of the $\lambda/4$ plate (in this experiment by 5°), such that near-zero optical transmission is realized. The THz wave will modify the probe beam ellipticity by a phase retardation $\Delta\phi$, and cause an increase or decrease of the transmitted probe beam energy $T_{\mathrm{EO}}(\tau)$, depending on the time delay τ between probe beam and THz pulse. For THz fields of equal but opposite magnitude, the change in transmission is not symmetric (not identical), but a well-known function of probe beam ellipticity [31]. For this reason the transmission measurement $T_{\mathrm{EO}}(\tau)$ was symmetrized using this function, yielding the EO signal $S_{\mathrm{EO}}(\tau)$.

There are several other EO-related effects that influence THz waveform analysis [30,32]: (1) The probe beam has a finite pulse length, limiting the temporal resolution of the EO method. (2) Dispersion and absorption in the ZnTe crystal causes THz pulse distortion. (3) There is a mismatch between the phase velocity of the individual THz frequencies and the group velocity of the probe beam. Since the ZnTe crystal has a well characterized dispersion function in both the near-infrared and THz spectral domain [30,33,34], these effects can be modeled and the original THz waveform $E_{\mathrm{THz}}(t)$ can be extracted from the measured (and symmetrized for probe beam ellipticity) EO signal $S_{\mathrm{EO}}(\tau)$. In the frequency domain, a slowly varying envelope approximation can be applied to the convolution of the probe beam and the THz waveform [32], yielding

$$S_{\mathrm{EO}}(\omega) \propto r_{41}(\omega) I_{\mathrm{pr}}(\omega) E_{\mathrm{THz}}(\omega) T_{\mathrm{ZnTe}}(\omega), \qquad (1)$$

with $\omega = 2\pi\nu$ the angular frequency, $I_{\mathrm{pr}}(\omega) = e^{-\omega^2\sigma_{\mathrm{pr}}^2/4}$, σ_{pr} the probe beam pulse length (rms), and $r_{41}(\omega)$ the EO coefficient. The crystal transfer function $T_{\mathrm{ZnTe}}(\omega)$ incorporates the dispersion, absorption, and mismatch. The inset in Fig. 2 shows the amplitude of the ZnTe transfer function (solid curve), the spectrum of the envelope of the probe beam $e^{-\omega^2\sigma_{\mathrm{pr}}^2/4}$ (dotted curve), as well as the theoretical curve for CTR from a 50 fs (rms) Gaussian electron bunch (dashed curve). Although a strong 5.3 THz phonon resonance exists [32], the effective cutoff frequency of the 200 μm-thick ZnTe crystal lies at 4 THz due to the velocity mismatch between THz and probe beam.

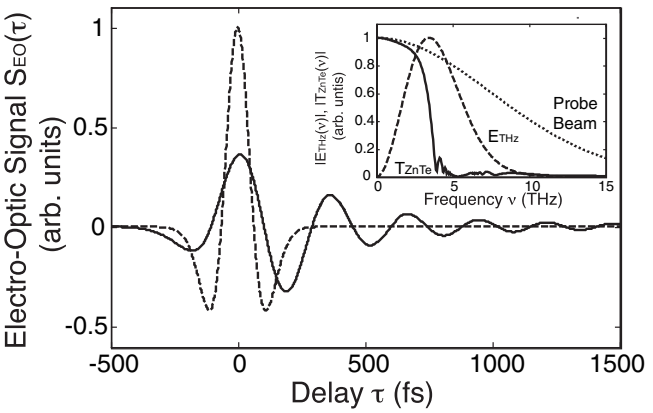

FIG. 2. The main plot shows the modeled EO signal $S_{\mathrm{EO}}(\tau)$ using a ZnTe crystal (solid curve) and using a dispersion-, absorption-, and mismatch-free crystal (dashed curve). In this model, the THz radiation is CTR from a 50 fs (rms) Gaussian electron bunch. The inset shows the amplitude of the CTR spectrum $|E_{\mathrm{THz}}(\nu)|$ (dashed curve), as well as the ZnTe transfer function $|T_{\mathrm{ZnTe}}(\nu)|$ (solid curve), and spectrum of the envelope of the probe beam (dotted curve).

The CTR characteristics can be modeled from the well-known angular and spectral distribution function for an electron passing a metal-vacuum boundary [26]. Concerning the LWFA, previous analysis [16] has shown that the plasma-vacuum boundary can be modeled as a metal-vacuum interface with a finite transverse size given by the transverse extent of the plasma. To include the coherence effects at the boundary, the angular and spectral distribution function is multiplied by the form factor $F(\omega)$ of the electron bunch and by the diffraction function $D(\omega)$ [16], such that the THz electric field is given by [17]

$$E_{\mathrm{THz}}(\omega) \propto \int g(u) \frac{u\sqrt{1+u^2}\sin\theta}{1+u^2\sin^2\theta} D(\omega, u) F(\omega, u) du, \quad (2)$$

where θ is the angle of emission with respect to the electron propagation axis, and $g(u)$ is the electron momentum distribution with u the electron momentum normalized to $m_e c$. Note that at small observation angles $\theta < 1$, the form factor $F(\omega)$ for LWFA-produced bunches is dominated by the temporal bunch profile since the transverse bunch size is smaller then the longitudinal bunch length. In the experimental setup, the observation angle was $\theta = 19°$. The CTR spectrum [inset of Fig. 2 (dashed curve)] is derived from a 50 fs (rms) Gaussian electron bunch, exiting a plasma with transverse radius of $\rho = 200$ μm (consistent with plasma density interferometry). The ZnTe-induced EO signal $S_{\mathrm{EO}}(\tau)$ from this bunch form, with $S_{\mathrm{EO}}(\tau)$ the inverse Fourier transformation of $S_{\mathrm{EO}}(\omega)$, is plotted as a solid curve in the main plot of Fig. 2. The dashed curve in the same plot indicates the EO signal through use of an ideal crystal (no mismatch, no dispersion, no absorption, and an ultrashort probe beam). The reflective THz losses at the crystal interface only significantly affect the amplitude of $S_{\mathrm{EO}}(\tau)$, and not the shape of the waveform, and are therefore ignored here.

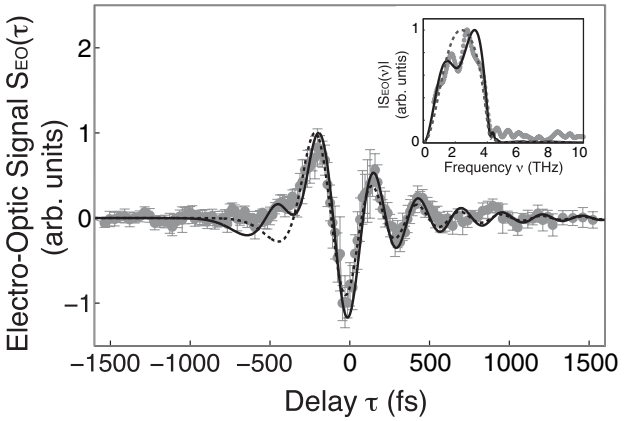

FIG. 3. The main plot shows the measured EO signal $S_{\mathrm{EO}}(\tau)$ (gray dots), with the black curves representing the modeled EO signal based on CTR from a single-bunch charge profile (dashed curve) and double-bunch profile (solid curve, with 30% of charge in leading bunch at 230 fs temporal separation). The length of each bunch in the model is set at 50 fs (rms). The Fourier transformation of the data (gray dots) and modeled waveforms are shown in the inset (solid curve for double-bunch profile, dashed curve for single-bunch profile).

The EO measurement, which is representative of several data sets, is shown in Fig. 3 as gray dots, where the measured EO signal $S_{\mathrm{EO}}(\tau)$ is plotted versus time delay. The delay stage was scanned with steps of 20 fs, and at each step 10 laser shots were taken, resulting in a 60 min long scan at 0.4 Hz system operation. The error bars represent the standard deviation on the 10 shots. The Fourier transformation of the data is plotted as gray dots in the inset of Fig. 3. Since a clean EO waveform was recorded in this single-diode EO configuration (no reference diode), where frequencies up to the 200 μm-thick ZnTe detection limit of 4 THz were fully resolved, a stable accelerator performance was demonstrated. Both figures in Fig. 3 also display a modeled EO signal $S_{\mathrm{EO}}(\tau)$ based on CTR from a Gaussian charge distribution (dashed black curves). A good fit is found for a 50 fs (rms) single bunch. Because of the 4 THz detection cutoff, we found that the charge profile could be shorter than 50 fs without significantly modifying the measured EO signal. However, if a longer charge profile is chosen, the theoretical curve no longer agrees with the measured sharp spectral cutoff at 4 THz.

Regarding the model based on CTR from a single bunch (dashed curves in Fig. 3), both a discrepancy between the temporal measurement and fit, as well as the presence of a spectral oscillation, can indicate that a more complex charge profile exists. For example, the modeled EO signal based on a double-bunch charge profile is shown as solid curves in Fig. 3, with both bunches Gaussian shaped (50 fs rms) and separated in time by 230 fs (30% of the charge in the first bunch). The double-bunch-based model results in an improved fit in the time domain, and the observed spectral oscillation (direct consequence of the double bunch) is reproduced. A possible mechanism for the double-bunch structure is plasma-gradient-induced wave breaking [35,36]. As the electron bunch and plasma wave propagate down the plasma density ramp (at the end of the gas jet, with a typical length of 100 μm), a second phase of electron trapping can occur several plasma wavelengths behind the leading bunch. The trapping occurs when the plasma fluid velocity matches the local phase velocity of the plasma wave, which is decreasing (due to the negative density gradient) as a function of distance behind the driver of the plasma wave. Alternatively, nonlinear transverse wave breaking [37] in the uniform-density part of the plasma could also lead to a second trapping phase several plasma wavelengths behind the leading bunch. In future experiments a single-shot EO technique [21] will be implemented, providing charge profile information for every shot instead of a temporal average as in the scanning technique.

An additional data set with a linear polarization state of the probe beam was recorded. In this measurement, the peak diode signal (maximal EO effect) showed a transmission of $T_{\mathrm{EO}} = 5.7 \times 10^{-3}$, where $T_{\mathrm{EO}} = 1$ represents

the total energy in the probe beam. The peak phase retardation $\Delta\phi$, induced by the THz pulse, is related to the peak transmission through $\Delta\phi \simeq 2\sqrt{T_{\mathrm{EO}}}$, resulting in $\Delta\phi \simeq 0.15$ rad. $\Delta\phi$ can be related to the incident peak THz field [29] through $\Delta\phi = 2\pi L n_0^3 r_{41} E_{\mathrm{THz}}/(\lambda_0\sqrt{\eta})$, with $n_0 = 2.85$ the refractive index for ZnTe at $\lambda_0 = 800$ nm, r_{41} the EO coefficient ($r_{41} \simeq 4.0 \times 10^{-12}$ m V^{-1} [38]), and $\eta \simeq 3$–6 the EO transmission reduction due to THz reflection at the crystal surface and THz pulse distortion in the ZnTe. The incident peak field was then $E_{\mathrm{THz}} = 18$–25 kV cm^{-1}.

Since OAP2 collects less than 5% of the originally radially polarized THz beam, higher peak fields could be realized through improved collection in future experiments. Furthermore, the generation of high-energy (>100 MeV) quasi-mono-energetic and low-divergence electron beams in a channel-guided LWFA, which has recently been demonstrated [8], could significantly boost peak fields of femtosecond THz (CTR) pulses. In such an experiment, CTR could be generated by propagating the electrons through a metallic foil (with reduced diffraction effects) downstream of the gas jet, and, since the CTR generation plane is spatially separated from the gas jet and remnant laser light, efficient THz collection can be realized. Transverse and longitudinal debunching are minimal for these low-energy-spread ultrarelativistic electron beams.

In summary, temporal characterization of laser-wakefield accelerated electron bunches has been performed through single-diode EO sampling of THz radiation, emitted by the electron bunch as it passes the plasma-vacuum interface. The data indicates the presence of 50 fs (rms) charge structure, since modeled CTR from a 50 fs (rms) Gaussian bunch results in a good fit with the data. Sub-50 fs bunch structure could be present, but the measurements were limited by the temporal resolution of the ZnTe crystal. Details of the EO waveform could suggest a more complex (non-Gaussian) charge profile, which might be characterized in future single-shot experiments. The shot-to-shot synchronization between electron and probe beam, combined with the stability of the electron beam properties are of sufficient performance to fully resolve CTR frequencies up to the 200 μm-thick ZnTe detection limit of 4 THz. Peak electric fields of the THz pulse in the range 18–25 kV cm^{-1} were observed.

The authors gratefully acknowledge contributions from J. Byrd, M. Martin, and Z. Hao on THz detection. This work was supported by the Director, Office of Science, Office of High Energy Physics, of the U.S. Department of Energy under Contract No. DE-AC02-05CH11231.

*Also at Eindhoven University of Technology, the Netherlands.
†Also at University of Paris XI, Orsay, France.

[1] T. Tajima and J. M. Dawson, Phys. Rev. Lett. **43**, 267 (1979).
[2] E. Esarey, P. Sprangle, J. Krall, and A. Ting, IEEE Trans. Plasma Sci. **24**, 252 (1996).
[3] A. Modena *et al.*, Nature (London) **377**, 606 (1995).
[4] A. Ting *et al.*, Phys. Plasmas **4**, 1889 (1997).
[5] V. Malka *et al.*, Science **298**, 1596 (2002).
[6] W. P. Leemans *et al.*, Phys. Rev. Lett. **89**, 174802 (2002).
[7] S. P. D. Mangles *et al.*, Nature (London) **431**, 535 (2004).
[8] C. G. R. Geddes *et al.*, Nature (London) **431**, 538 (2004).
[9] J. Faure *et al.*, Nature (London) **431**, 541 (2004).
[10] K.-C. Tzeng, W. B. Mori, and T. Katsouleas, Phys. Rev. Lett. **79**, 5258 (1997).
[11] E. Esarey, B. Hafizi, R. Hubbard, and A. Ting, Phys. Rev. Lett. **80**, 5552 (1998).
[12] W. P. Leemans *et al.*, Phys. Plasmas **8**, 2510 (2001).
[13] E. Esarey, B. A. Shadwick, P. Catravas, and W. P. Leemans, Phys. Rev. E **65**, 056505 (2002).
[14] A. Rousse *et al.*, Phys. Rev. Lett. **93**, 135005 (2004).
[15] W. P. Leemans *et al.*, Phys. Rev. Lett. **91**, 074802 (2003).
[16] C. B. Schroeder, E. Esarey, J. van Tilborg, and W. P. Leemans, Phys. Rev. E **69**, 016501 (2004).
[17] J. van Tilborg, C. B. Schroeder, E. Esarey, and W. P. Leemans, Laser Part. Beams **22**, 415 (2004).
[18] X. Yan *et al.*, Phys. Rev. Lett. **85**, 3404 (2000).
[19] M. J. Fitch, A. C. Melissinos, P. L. Colestick, and W. H. Hartung, Phys. Rev. Lett. **87**, 034801 (2001).
[20] I. Wilke *et al.*, Phys. Rev. Lett. **88**, 124801 (2002).
[21] G. Berden *et al.*, Phys. Rev. Lett. **93**, 114802 (2004).
[22] A. L. Cavalieri, D. M. Frits, S. H. Lee, P. H. Bucksbaum, and J. B. Hastings, Phys. Rev. Lett. **94**, 114801 (2005).
[23] U. Happek, A. J. Sievers, and E. B. Blum, Phys. Rev. Lett. **67**, 2962 (1991).
[24] Y. Shibata *et al.*, Phys. Rev. E **50**, 1479 (1994).
[25] P. Kung, H.-C. Lihn, H. Wiedemann, and D. Bocek, Phys. Rev. Lett. **73**, 967 (1994).
[26] M. L. Ter-Mikaelian, *High-Energy Electromagnetic Processes in Condensed Media* (Wiley, New York, 1972).
[27] W. P. Leemans *et al.*, Phys. Plasmas **11**, 2899 (2004).
[28] J. A. Valdmanis, G. Mourou, and C. W. Gabel, Appl. Phys. Lett. **41**, 211 (1982).
[29] A. Yariv, *Quantum Electronics* (Wiley, New York, 1988).
[30] J. Faure, J. van Tilborg, R. A. Kaindl, and W. P. Leemans, Opt. Quantum Electron. **36**, 681 (2004).
[31] Z. Jiang, F. G. Sun, Q. Chen, and X.-C. Zhang, Appl. Phys. Lett. **74**, 1191 (1999).
[32] G. Gallot and D. Grischkowsky, J. Opt. Soc. Am. B **16**, 1204 (1999).
[33] G. Gallot, J. Zhang, R. W. McGowan, T. Jeon, and D. Grischkowsky, Appl. Phys. Lett. **74**, 3450 (1999).
[34] D. T. F. Marple, J. Appl. Phys. **35**, 539 (1964).
[35] S. Bulanov, N. Naumova, F. Pegoraro, and J. Sakai, Phys. Rev. E **58**, R5257 (1998).
[36] P. Tomassini *et al.*, Phys. Rev. ST Accel. Beams **6**, 121301 (2003).
[37] S. V. Bulanov, F. Pegoraro, A. M. Pukhov, and A. S. Sakharov, Phys. Rev. Lett. **78**, 4205 (1997).
[38] Q. Wu and X.-C. Zhang, Appl. Phys. Lett. **68**, 1604 (1996).